

Symmetry transformation of nonlinear optical current of tilted Weyl nodes and application to ferromagnetic $MnBi_2Te_4$

Zhuo-Cheng Lu(卢倬成) and Ji Feng(冯济)

Citation: Chin. Phys. B, 2024, 33 (**4**): 047303. DOI: 10.1088/1674-1056/ad2bfb
Journal homepage: http://cpb.iphy.ac.cn; http://iopscience.iop.org/cpb

What follows is a list of articles you may be interested in

Nonlinear current response and electric quantum oscillations in the Dirac semimetal Cd_3As_2

Hao-Nan Cui(崔浩楠), Ze-Nan Wu(吴泽南), Jian-Kun Wang(王建坤), Guang-Yu Zhu(祝光宇), Jia-Jie Yang(杨佳洁), Wen-Zhuang Zheng(郑文壮), Zhi-Min Liao(廖志敏), Shuo Wang(王硕), Ben-Chuan Lin(林本川), and Dapeng Yu(俞大鹏)

Chin. Phys. B, 2023, 32 (**8**): 087306. DOI: 10.1088/1674-1056/acd9c5

Negative magnetoresistance in Dirac semimetal Cd_3As_2 with in-plane magnetic field perpendicular to current

Hao-Nan Cui(崔浩楠), Guang-Yu Zhu(祝光宇), Jian-Kun Wang(王建坤), Jia-Jie Yang(杨佳洁), Wen-Zhuang Zheng(郑文壮), Ben-Chuan Lin(林本川), Zhi-Min Liao(廖志敏), Shuo Wang(王硕), and Da-Peng Yu(俞大鹏)

Chin. Phys. B, 2023, 32 (**7**): 077305. DOI: 10.1088/1674-1056/accd50

Large positive magnetoresistance in photocarrier-doped potassium tantalites

Rui-Shu Yang(杨睿姝), Ding-Bang Wang(王定邦), Yang Zhao(赵阳), Shuan-Hu Wang(王拴虎), and Ke-Xin Jin(金克新)

Chin. Phys. B, 2022, 31 (**12**): 127302. DOI: 10.1088/1674-1056/ac6742

Hydrodynamic simulation of chaotic dynamics in InGaAs oscillator in terahertz region

Wei Feng(冯伟)

Chin. Phys. B, 2020, 29 (**4**): 047302. DOI: 10.1088/1674-1056/ab696f

Topological transport in Dirac electronic systems: A concise review

Hua-Ding Song(宋化鼎), Dian Sheng(盛典), An-Qi Wang(王安琦), Jin-Guang Li(李金光), Da-Peng Yu(俞大鹏), Zhi-Min Liao(廖志敏)

Chin. Phys. B, 2017, 26 (**3**): 037301. DOI: 10.1088/1674-1056/26/3/037301

RAPID COMMUNICATION

Symmetry transformation of nonlinear optical current of tilted Weyl nodes and application to ferromagnetic $MnBi_2Te_4$

Zhuo-Cheng Lu(卢倬成) and Ji Feng(冯济)[†]

International Center for Quantum Materials, School of Physics, Peking University, Beijing 100871, *China*

(Received 12 December 2023; revised manuscript received 17 February 2024; accepted manuscript online 22 February 2024)

A Weyl node is characterized by its chirality and tilt. We develop a theory of how *n*th-order nonlinear optical conductivity behaves under transformations of anisotropic tensor and tilt, which clarifies how chirality-dependent and -independent parts of optical conductivity transform under the reversal of tilt and chirality. Built on this theory, we propose ferromagnetic $MnBi_2Te_4$ as a magnetoelectrically regulated, terahertz optical device, by magnetoelectrically switching the chirality-dependent and -independent DC photocurrents. These results are useful for creating nonlinear optical devices based on the topological Weyl semimetals.

Keywords: nonlinear optical response, topological Weyl semimetals, chiral anomaly

PACS: 73.50.Fq, 73.43.Qt, 71.55.Ak, 73.63.–b **DOI:** 10.1088/1674-1056/ad2bfb

1. Introduction

The gapless excitations make Weyl semimetals an ideal platform to perform low-energy photon detection, particularly in the infrared and terahertz regimes.[1] Various nonlinear optical responses, such as harmonic generations,[2–5] bulk photovoltaic effect[6–11] and four-wave mixing,[12,13] have been widely studied in Weyl semimetals. Furthermore, it has recently been recognized that the geometry and topology of electronic band structures can have nontrivial impacts on optical conductivities. Nonlinear optical effects like bulk photovoltaic effects and harmonic generations can be described using topological quantities involving Berry connection and curvature, which provide a unified perspective on various optical phenomena.[14,15] The circular photogalvanic effect in Weyl semimetals, for instance, is recognized as a direct measurement of the topological charge of Weyl nodes and exhibits material-independent quantization.[6] Additionally, the giant optical response of Weyl semimetals attributing to singularity enhancement by geometric quantities has been studied theoretically and experimentally.[8,10] As a result, Weyl semimetals have garnered substantial attention as materials of choice for exploring innovative optoelectronic devices.

Weyl nodes show up in pairs due to the no-go theorem,[16] and there can be as many as 160 pairs in a Weyl semimetal.[17] Oftentimes, the Weyl nodes in one material can be interrelated by discrete symmetries, including rotations (proper or improper) and time-reversal, which furnishes links between optical responses between symmetry-related Weyl nodes. On the other hand, when analyzing the optical response for a single Weyl node, the symmetry of the system (with all the nodes) is unspecified. It might be straightforward to work out the relation between the optical conductivities of a pair of nodes related by rotations. However, things become obscure when it comes to symmetry operations involving time-reversal, and the difficulty arises from dissipation.[8] Therefore, such symmetry analysis requires knowledge of a microscopic expression of optical conductivities. For nonlinear optical conductivities, the microscopic theory can be fairly complicated and involves multiple terms that transform differently under time-reversal. A theory to link the optical conductivities related by discrete symmetries, including rotation and time-reversal, is evidently needed.

A Weyl node in Weyl semimetals is characterized primarily by its chirality and tilt.[18,19] In relation to optical responses, the chirality of a Weyl node determines the geometric quantities (matrix elements) that enter into the photocurrent, whereas the tilt of the spectrum determines the phase space of the electron–hole response. For instance, it has been demonstrated that finite tilt is important to generate a giant photocurrent.[7] And the bulk photovoltaic effect shows different behavior in low frequencies for type I and type II Weyl semimetals.[9] Although it is believed that the chirality and tilt of a Weyl node have significant impacts on the direction and magnitude of photocurrent, how these basic characteristics of symmetry-related Weyl nodes reveal the relations of their nonlinear optical conductivities remains to be systematically understood. These types of relations have been largely overlooked so far because they are generally inaccessible from experiments since Weyl nodes always appear in pairs and multiple Weyl nodes usually contribute to the total optical response. However, the optical response of a single Weyl node could be interesting when the degeneracy of Weyl pairs is lifted.

[†]Corresponding author. E-mail: jfeng11@pku.edu.cn

© 2024 Chinese Physical Society and IOP Publishing Ltd

For example, the optical response of Weyl semimetals could come from only a single Weyl node with nonzero chirality imbalance.[20,21] Therefore, precise statements of these types of relations are useful for further exploration of the potential optical devices based on the nonlinear optical response of Weyl nodes.

In this work, we systematically investigate how the tilt and chirality of Weyl nodes together affect the sign and magnitude of the nonlinear photocurrent. In Section 2, we discuss how to relate the transformation W connecting the effective Hamiltonians of two Weyl nodes to their optical conductivity. We propose that a general nth-order optical conductivity of Weyl nodes can be decomposed as a chirality-independent part σ_0 and a chirality-dependent part σ_χ according to space–time inversion $P\Theta$. We also discuss their distinct geometric interpretations and show a sign-change rule of σ_0 and σ_χ when reversing the tilt in a certain direction. We further demonstrate the contrasting behaviors of σ_0 and σ_χ for odd (or even) orders when reversing the tilt or chirality, which can be generalized to multi-Weyl nodes. In Section 3, based on our theory, we propose ferromagnetic $MnBi_2Te_4$ as a magnetoelectrically regulated optical device that carries two components of photocurrent j_0 and j_χ, the directions of which are controlled by external electromagnetic fields. Valid parameters for experimental measurements are also discussed based on the effective Hamiltonian of the Weyl node with Landau levels.

2. Optical conductivities of a general Weyl node

Since a generic Weyl node is characterized solely by its chirality and tilt, it would be desirable to understand how these quantities alone, without having to consult the overall symmetry, impact the photocurrent. Although symmetry analysis is very useful in singling out zero elements in the optical conductivity tensors, this is no longer the case if we focus on the optical response of a single Weyl node. With a single Weyl node, the full symmetry of the system is unspecified, and there could be emerging symmetry at low energies. The low-energy effective Hamiltonian has the form[18] of

$$\mathcal{H}(\boldsymbol{k};\boldsymbol{t},\boldsymbol{A}) = t_a k_a + k_a A_{ab}\tau_b, \tag{1}$$

where indices $a,b = x,y,z$ (summation implied when repeated), $\boldsymbol{k}$ is the wavevector, and τ_b's are the Pauli matrices. The non-singular matrix A_{ab} is referred to as the anisotropic tensor, and correspondingly, $\chi = \det \boldsymbol{A}/|\det \boldsymbol{A}| = \pm 1$ is the chirality of the Weyl node. The energy spectrum is $\varepsilon_s(\boldsymbol{k}) = k_a t_a + s|k_a A_{ab}|$, where $s = \pm$ corresponds to conduction and valence bands, respectively. The vector $\boldsymbol{t}$ tilts the Weyl node, determining the shape of the Fermi surface. If $|t_a k_a| < / > |k_a A_{ab}|$ when $\boldsymbol{k}$ is along the tilt direction, the system is a type-I/type-II Weyl semimetal. A type-I Weyl semimetal has a closed Fermi surface, whereas a type-II Weyl semimetal has a Fermi surface comprised of electron and hole pockets.[19] Under the symmetry transformation, $\boldsymbol{k}$ operates as a polar c-vector, while $\boldsymbol{\tau}$ functions as an axial c-vector. In this context, i-/c-vectors are time-reversal symmetric/antisymmetric respectively. Consequently, Weyl nodes associated by inversion manifest opposite tilt and chirality. On the other hand, Weyl nodes linked by time-reversal display opposite tilt while preserving the same chirality. Analogous analyses can be applied to the cases of Weyl nodes associated by other symmetries. Below, we will reveal how $\boldsymbol{t}$ and $\boldsymbol{A}$ impact the general nth-order photocurrent from a Weyl node described by Eq. (1).

The photocurrent arises from the incident light's electric field, which is a superposition of multiple frequency components $E_a(t) = E_a^\gamma \mathrm{e}^{-\mathrm{i}\omega_\gamma t}$, where the frequency component γ is summed over implicitly when repeated. Here, E_a^γ is independent of position under the long-wavelength limit. For a Weyl node described by Eq. (1), the total nth-order photocurrent j_a with a frequency ω_n can be expressed as

$$j_a^{(n)}(\omega_n) = \sum_{C(\omega_n)} \sigma^{ab_1\cdots b_n}(\omega_n;\omega_{\gamma_1}\cdots\omega_{\gamma_n}) E_{b_1}^{\gamma_1}\cdots E_{b_n}^{\gamma_n}, \tag{2}$$

where $\omega_n = \omega_{\gamma_1} + \cdots + \omega_{\gamma_n}$, and $\sigma^{ab_1\cdots b_n}(\cdots)$ is the nth-order conductivity tensor. The set $C(\omega_n)$ collects all possible selections of n frequencies that sum to ω_n. Based on the length-gauge theory of nonlinear optical response,[22,23] the nth-order optical conductivity in Eq. (2) can be generally written as

$$\sigma^{ab_1\cdots b_n} = \int [\mathrm{d}\boldsymbol{k}] \Sigma^{ab_1\cdots b_n}(\boldsymbol{k}), \tag{3}$$

in which we have omitted frequency variables and $[\mathrm{d}\boldsymbol{k}] = \mathrm{d}^3k/(2\pi)^3$. It is worth noting that the integrand $\boldsymbol{\Sigma}$ is a gauge-invariant tensor, whose tensor component arises from the k_b-derivative, ∂_{k_b}. For concreteness, a detailed discussion of why the nth-order optical conductivity can be written in the form of Eq. (3) is presented with examples in Appendix A.

For two Weyl nodes $\mathcal{H}$ and $\mathcal{H}'$ related through the transformation $\mathcal{H} \mapsto \mathcal{H}' : k_b \mapsto k_a W_{ab}$, we find their nonlinear optical conductivities, as described by Eq. (3), have the following relationship:

$$\sigma^{ab_1\cdots b_n}(\mathcal{H}') = \sigma^{a'b_1'\cdots b_n'}(\mathcal{H}) \frac{W_{aa'}W_{b_1b_1'}\cdots W_{b_nb_n'}}{|\det W|}, \tag{4}$$

in which we assume the same chemical potentials. The product of $W_{bb'}$ factors arises from the transformation of derivatives ∂_{k_b}. The factor of $|\det W|$ comes from the Jacobian of the momentum integral. Transformation W is spatial since it only affects $\boldsymbol{k}$. If $|\det W| = 1$, W corresponds to a certain spatial symmetry operation. As a simple example, when $W_{bb'} = -\delta_{bb'}$, Eq. (4) describes the relationship between the optical conductivities of two Weyl nodes connected by inversion P, which is $\sigma^{ab_1\cdots b_n}(\mathcal{H}') = (-1)^{n+1}\sigma^{ab_1\cdots b_n}(\mathcal{H})$, where n represents the order of response. It is essential to note that Eq. (4) discusses the relationship between the optical conductivities of two Weyl

nodes in the same spacetime, rather than the correspondence of the optical conductivity of a single Weyl node in two different spacetime coordinates. Equation (4) establishes a connection between the transformation W applied to the effective Hamiltonian of the Weyl node and the associated nth-order optical conductivity. Consequently, Eq. (4) can serve as a tool for studying the nonlinear optical properties of Weyl nodes.

In Eq. (4), both tilt and chirality are affected by the transformation W. For further isolation of the impacts of the transformations of tilt and chirality on the optical conductivity, we note that the nth-order optical conductivity for a Weyl node described by Eq. (1) can be decomposed as

$$\sigma^{ab_1\cdots b_n} = \sigma_0^{ab_1\cdots b_n} + \sigma_\chi^{ab_1\cdots b_n}, \tag{5}$$

where the first term σ_0 is chirality-independent, whereas the second term σ_χ reverses sign upon chirality reversal, i.e., $\boldsymbol{A} \mapsto -\boldsymbol{A}$. Furthermore, we recognize that two Weyl nodes related by space–time inversion $P\Theta$ have the same $\boldsymbol{t}$, while their $\boldsymbol{A}$ differ by a sign. Therefore, we identify σ_0 as the portion that remains unchanged under $P\Theta$, while σ_χ represents the portion that changes sign under $P\Theta$. Additionally, the distinction between σ_0 and σ_χ is closely related to their different geometric interpretations. From the discussions in Appendix A, we can see that quantity $r^a_{nm}r^b_{mn}$ (r^a_{nm} is the interband Berry connection) is widely involved in the first-order to third-order optical conductivities. This quantity has a geometric interpretation of band-resolved quantum geometric tensor, which can be decomposed as $r^a_{nm}r^b_{mn} = g^{ab}_{nm} - (\mathrm{i}/2)\Omega^{ab}_{nm}$.[8,24] g^{ab}_{nm} is the symmetric part that corresponds to the band-resolved quantum metric, while the antisymmetric part Ω^{ab}_{nm} is the band-resolved Berry curvature. Their names come from the fact that the Berry curvature and quantum metric can be recovered by summing over band m, $g^{ab}_n = \sum_{m\neq n} g^{ab}_{nm}$ and $\Omega^{ab}_n = \sum_{m\neq n}\Omega^{ab}_{nm}$. The quantum metric is a chirality-independent quantity since it can be interpreted as the distance between different quantum states. On the other hand, the Berry curvature reverses sign when chirality changes, since Weyl nodes with $\chi = \pm 1$ correspond to the source (or sink) of Berry curvature in k space. Here, we emphasize that σ_0/σ_χ does not necessarily correspond to the band-resolved quantum metric/Berry curvature. The specific correspondence should be determined through a symmetry analysis of the microscopic conductivity expressions, which is discussed with examples in Appendix B.

Equation (5) discusses the impact of chirality changes on optical conductivity. Next, we want to explore the influence of tilt variations on optical conductivity. Without loss of generality, we can always choose a coordinate system where $\boldsymbol{A}$ is diagonal. In such a scenario, we discover that two Weyl nodes, possessing the same $\boldsymbol{A}$ and tilts that are identical across all components except for an opposite c component, are linked by the symmetry operation $\mathcal{M}_c = M_c P\Theta$, where M_c is mirror reflection in c direction. Aided by Eqs. (4) and (5), we ascertain that the optical conductivities of these two Weyl nodes relate as follows:

$$\begin{aligned}\sigma_0^{ab_1\cdots b_n}(\mathcal{M}_c\mathcal{H}\mathcal{M}_c^\dagger) &= (-1)^{\alpha_c}\sigma_0^{ab_1\cdots b_n}(\mathcal{H}),\\ \sigma_\chi^{ab_1\cdots b_n}(\mathcal{M}_c\mathcal{H}\mathcal{M}_c^\dagger) &= (-1)^{\alpha_c+1}\sigma_\chi^{ab_1\cdots b_n}(\mathcal{H}),\end{aligned} \tag{6}$$

in which α_c marks how many times c appears in superscript $ab_1\cdots b_n$. In Eq. (6), σ_0 and σ_χ exhibit distinct changes when $t_c \to -t_c$. This arises from the fact that chirality changes sign under $P\Theta$. Equation (6) can be helpful when we study the nonlinear optical conductivities of two Weyl nodes related to each other by transformation $t_c \mapsto -t_c$ dictated by the symmetry relating the Weyl pair. In particular, for a Weyl node with $t_c = 0$, $t_c \mapsto -t_c$ will immediately reveal the selection rule for $\sigma_0^{ab_1\cdots b_n}/\sigma_\chi^{ab_1\cdots b_n}$.

Table 1. Transformations of nth-order optical conductivities of a Weyl node under Θ, P, and $P\Theta$. Since these transformations depend only on whether the order of response is even or odd, we use $\sigma^{\mathrm{odd/even}}$ to denote the tensor for an odd/even-order response. The plus (minus) one below $\boldsymbol{t}/\boldsymbol{A}/\boldsymbol{\sigma}$ means the sign of tilt/chirality/conductivities is unchanged (reversed) under the corresponding symmetry operation. We observe that, σ_0^{odd} is insensitive to the reversal of tilt and chirality, while $\sigma_\chi^{\mathrm{odd}}$ changes sign due to the reversal of tilt or chirality. On the other hand, the sign of $\sigma_0^{\mathrm{even}}/\sigma_\chi^{\mathrm{even}}$ exclusively depends on the tilt/chirality.

	$(\boldsymbol{t},\boldsymbol{A})$	σ_0^{odd}	$\sigma_\chi^{\mathrm{odd}}$	σ_0^{even}	$\sigma_\chi^{\mathrm{even}}$
Θ	$(-1,+1)$	$+1$	-1	-1	$+1$
P	$(-1,-1)$	$+1$	$+1$	-1	-1
$P\Theta$	$(+1,-1)$	$+1$	-1	$+1$	-1

Let us comment on how the results can be useful in analyzing optical responses in Weyl semimetals, before going to concrete examples. Using Eqs. (4)–(6), we can quickly determine whether a conductivity tensor component of a Weyl node should be zero and whether it corresponds to σ_0 or σ_χ. This leads to the knowledge that how optical conductivities of a symmetry-related Weyl pair are interrelated based solely on $\boldsymbol{t}$ and $\boldsymbol{A}$. In particular, this is made possible regardless of the frequency-dependence of the optical conductivity tensor and whether the Weyl nodes are type-I or type-II. These are done without requiring the knowledge of complete symmetry of the Weyl nodes or recourse to microscopic expressions of the conductivities even if the symmetry operation involves time-reversal. As a quick demonstration, we can work out how the conductivities of a Weyl node transform under time-reversal Θ, inversion P, and the space–time inversion $P\Theta$, as shown in Table 1. According to Eq. (5), $P\Theta$ changes the sign of σ_χ while keeping σ_0 unchanged. On the other hand, according to Eq. (6), Θ changes the sign of $\sigma_\chi^{\mathrm{odd}}$ and σ_0^{even}, while keeping $\sigma_\chi^{\mathrm{even}}$ and σ_0^{odd} unchanged. Then, how σ_0 and σ_χ change under P can be directly deduced from the composite operation of $P\Theta$ and Θ. It should be noted that results in Table 1 are also a consequence of how σ_0 and σ_χ transform under reversal of chirality and how the nth-order optical conductivity

transforms under P. Before ending this section, we emphasize the results in Eqs. (5) and (6) and Table 1 can be generalized to the multi-Weyl nodes.[25,26] The detailed discussion is presented in Appendix C.

3. Magnetoelectric switch

The foregoing analysis highlights the possibility of controlling the total photocurrent of the system by switching the Weyl nodes with different combinations of tilt and chirality. In this section, we propose a mechanism for magnetoelectrically switching using Weyl semimetals, making use of the formulas we developed in the last section. We consider a magnetic Weyl semimetal with a pair of Weyl nodes, dubbed I and II, interrelated by inversion. Suppose the material is a soft magnet whose magnetization can be easily trained by an external magnetic field $\boldsymbol{B}$. Without loss of generality, node I tilts along positive z-direction and with a chirality $\chi = +1$, and correspondingly node II tilts in negative z-direction with $\chi = -1$. Upon magnetization reversal by reversing the B-field, node I/II becomes its time-reversal counterparts I′/II′, which have opposite tilt and the same chirality. We also introduce an external DC electric field $\boldsymbol{E}_{\rm DC}$ that is parallel (or antiparallel) to $\boldsymbol{B}$, which together with the B-field can induce a chemical potential difference within a pair of Weyl nodes at steady states,

$$\delta\mu = \mu_{\rm I/I'} - \mu_{\rm II/II'} \propto \boldsymbol{E}_{\rm DC}\cdot\boldsymbol{B}, \tag{7}$$

owing to the chirality imbalance originating from chiral anomaly.[20,21] Then for a given incident photon energy $\hbar\omega$, we can combine the chirality imbalance with the Pauli blocking to selectively activate Weyl node for photocurrent. As schematically depicted in Fig. 1, the vertical electron–hole excitations are allowed (solid orange arrows)/forbidden (dashed light orange arrows) for activated/deactivated Weyl node when an appropriate $\hbar\omega$ is considered. Therefore, chirality imbalance can work as a switch of the optical response of nodes I, II, I′ and II′ by reversing the directions of B-field and $E_{\rm DC}$-field, which makes it possible for us to control the sign of tilt and chirality of Weyl node for photocurrent. In the setup depicted, I or I′ is activated for $\delta\mu < 0$, and II or II′ is activated for $\delta\mu > 0$. An important observation from Table 1 is that $\sigma_0^{\rm even}$ transforms as $\boldsymbol{t}$, and $\sigma_\chi^{\rm even}$ transforms as $\boldsymbol{A}$. Consequently, by selectively activating the Weyl node with B-field and $E_{\rm DC}$-field, a magnetoelectric switch can be envisioned that couples the tilt and chirality of the Weyl node to the direction of its second-order photocurrent.

The magnetoelectrically switching mechanism described above may be realized in ferromagnetic $MnBi_2Te_4$. Though the ground state of $MnBi_2Te_4$ is an antiferromagnetic topological insulator,[27–29] ferromagnetic $MnBi_2Te_4$ is believed to host many different topological phases including axion insulator, 3D Chern insulator, 3D quantum spin Hall insulator and Weyl semimetal by manipulating the magnetization and relative spacing.[30] Under high magnetic field, ferromagnetic $MnBi_2Te_4$ is computationally predicted to be Weyl semimetal that has only a pair of Weyl nodes,[27,29] supported by preliminary experimental data.[31] $MnBi_2Te_4$ comprises negatively charged Bi–Te layers neutralized with intercalated magnetic Mn cations in hexagonal close packing, as shown in Fig. 2(a). When the B-field aligns the magnetic moments in z-direction, the magnetic point group of ferromagnetic $MnBi_2Te_4$ is $\bar{3}m'$, and the pair of Weyl nodes, which can be marked as I and II, are bound to the high-symmetry k_z axis and tilt oppositely in the z-direction. Reversal of the B-field brings about Weyl nodes I′ and II′, which are the time-reversal images of I and II, respectively. The tilt directions and chiralities of I, II and their time-reversal images are the same as those previously proposed. In the following discussions, we will consider ferromagnetic $MnBi_2Te_4$ magnetized along $\pm z$-direction only.

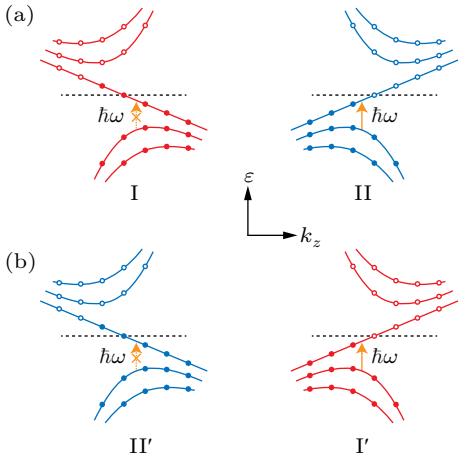


Fig. 1. Schematic of the switching mechanism of the photocurrent by chirality imbalance. Nodes I and II are depicted in panel (a) while nodes II′ and I′ are depicted in panel (b). A Weyl node is colored red/blue to indicate positive/negative chirality. Solid circles indicate occupied states while hollow circles indicate unoccupied states. Owing to the chiral magnetic field, each pair of nodes is differently populated. The black dashed line indicates the Fermi level without chirality imbalance. The solid/dashed orange arrows indicate the optical transitions are allowed/banned.

The electronic structure of ferromagnetic $MnBi_2Te_4$ is shown in Fig. 2(b). Weyl nodes I and II are on the high symmetric lines $\bar{Z}$–Γ–Z. When reversing the direction of the B-field, the spectrum stays unchanged while the chirality of Weyl nodes is switched. First-principles calculations were performed using Vienna *ab initio* simulation package equipped with the projector-augmented-wave potentials.[32] For structural relaxation, the exchange–correlation interactions were considered in the generalized gradient approximation (GGA) with the Perdew–Burke–Ernzerhof scheme.[33] For self-consistent calculation and band structure calculation, we consider the modified Becke–Johnson method. The correlation of 3d orbitals of Mn is partially treated with GGA + U formalism, with an isotropic $U = 4.0$ eV. The spin–orbital cou-

pling is included in self-consistant calculations. A 350 eV cut-off energy and $6\times6\times6$ $\boldsymbol{k}$-point sampling are considered.

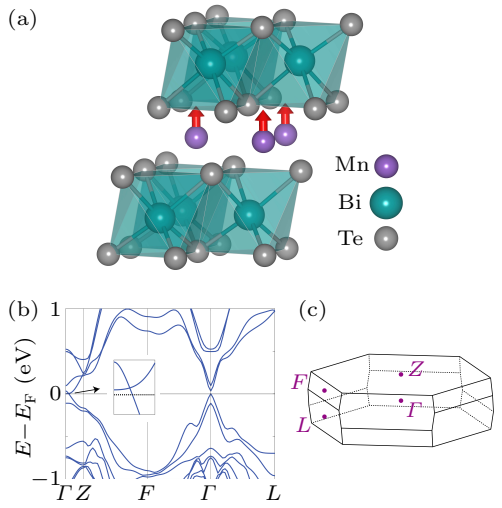


Fig. 2. Crystal and magnetic structures of ferromagnetic $MnBi_2Te_4$ are shown in panel (a), and the DFT band structure in a 2 eV window around the Fermi level is shown in panel (b). (a) The red arrows represent magnetic moments on Mn. (b) The DFT band structure is shown as blue lines. Weyl node II on the high symmetric lines Γ–Z are zoomed in and shown in the inset. I relates to II by inverison. (c) The high symmetry points are exhibited in the Brillouin zone with purple dots.

Since the ferromagnetic phase of $MnBi_2Te_4$ requires at least a 7.7 T B-field,[34] the effect of Landau levels should be considered. We fit the parameters of the low-energy effective Hamiltonian of Weyl nodes with the DFT band structure of ferromagnetic $MnBi_2Te_4$. Introducing the B-field in z-direction with vector potential $\boldsymbol{a}=Bx\hat{y}/\hbar$, the Weyl nodes then can be described by

$$\mathcal{H}=tv_tk_z+\chi[v_\parallel k_z\sigma_z+v_\perp(k_x\sigma_x+(k_y+ea_y)\sigma_y)]. \tag{8}$$

Fermi velocities in the plane are the same because of three-fold rotational symmetry along z-direction. $v_t=0.494$ eV·Å, $v_\parallel=0.625$ eV·Å and $v_\perp=1.975$ eV·Å. $t=+1$ for nodes I and II$'$ while $t=-1$ for nodes II and I$'$. $\chi=+1$ for nodes I and I$'$ while $\chi=-1$ for nodes II and II$'$. Here, the electron charge is $-e$ (i.e., $e>0$). Since the two Weyl nodes are well-separated in momentum space, the relaxation time of chirality-violating scattering τ_{cv} is much larger than that of chirality-preserving scattering τ_{cp}. At steady states, the chiral anomaly can be treated as the shift of chemical potential $\chi\delta\mu/2$ for the two Weyl nodes. Then, the chemical potential of Weyl nodes is $\mu=\mu_0+\chi\delta\mu/2$ with $\mu_0=-6$ meV being the chemical potential without chirality imbalance. Validation of this treatment is discussed in Appendix D. The energy of the nth (n is an integer) Landau level at $\boldsymbol{k}=[k_y,k_z]$ is

$$\varepsilon_{n\boldsymbol{k}}=tv_tk_z+\chi\,\mathrm{sgn}(n)\eta_n, \tag{9}$$

in which $\eta_n=\sqrt{2|n|\hbar^2v_\perp^2/\ell^2+\eta_\parallel^2}$ $(n\neq0)$, $\ell=\sqrt{\hbar/eB}$ is the magnetic length, $\eta_0=\eta_\parallel=v_\parallel k_z$, and the sign function $\mathrm{sgn}(n)$ equals -1 if $n=0$. The details of calculations of eigenfunctions and velocity matrix elements are presented in Appendix E, from which we can see that the optical transitions are nonzero only between Landau levels that satisfy $|m|-|n|=\pm1$.

Now, we are in a position to verify our proposal of magnetoelectrically regulated photocurrent in ferromagnetic $MnBi_2Te_4$. For a straightforward DC measurement, we consider that the system is illuminated by light propagating in z-direction. The optical electric field can be written as $E(t)=|E|(\cos\omega t,\eta\sin\omega t,0)$. The incident light is linearly polarized when $\eta=0$, or circular if $\eta=\pm1$, or elliptical somewhere in between. The optical electric field $E(t)$ has no contributions to the chiral anomaly since it is perpendicular to the B-field. The total DC current in z-direction has two components j_z^{stat} and j_z^{opt}. j_z^{stat} depends only on the E_{DC}-field while j_z^{opt} arises from the illumination of light. j_z^{stat} can be taken as background, because it is insensitive to the change of light. Since the two Weyl nodes are located on the high-symmetry line $\bar{Z}$–Γ–Z, the surface normal to z-direction is topologically trivial. This fact sparses us from distinguishing the responses from bulk Weyl nodes and topological surface states. A more detailed discussion is presented in Appendix F. Then, the dominant DC current flows in z-direction comes from the photovoltaic effect of the activated Weyl nodes, that is

$$j_z^{(2)}(\eta)=j_0+\eta j_\chi, \tag{10}$$

with $j_0\equiv\tilde{\sigma}_0|E|^2=(\sigma_0^{zxx}+\sigma_0^{zyy})|E|^2$ and $j_\chi\equiv\tilde{\sigma}_\chi|E|^2=\mathrm{i}(\sigma_\chi^{zyx}-\sigma_\chi^{zxy})|E|^2$. Other optical conductivity components are zero for Weyl nodes tilting in z-direction and $\boldsymbol{A}$ is diagonal according to Eq. (6). Therefore, the validation of magnetoelectrically regulated photocurrent in ferromagnetic $MnBi_2Te_4$ is verified, since direction of the photocurrent j_0/j_χ is determined exclusively by the tilt/chirality, and j_0 and j_χ can be distinguished by varying η. The proposed magnetoelectric switch based on ferromagnetic $MnBi_2Te_4$ is an illustration of analyzing the photocurrent using our result introduced in Section 2, without the knowledge of the complete symmetry of the Weyl nodes.

Next, we would like to discuss the experimental parameters of magnetoelectric switch by computing the second-order DC photocurrent of Weyl nodes in ferromagnetic $MnBi_2Te_4$. Based on the length-gauge theory of nonlinear optical response, dominant contributions of the photogalvanic effect are from the injection current and shift current in the clean limit.[22,23] Upon comparing the results presented in Table 1 with the symmetry analysis of injection current and shift current,[8] we observe that the circular shift current and linear injection current correspond to σ_0, while linear shift current and circular injection current correspond to σ_χ. Further, referring to Eq. (10), we note that only the linear injection current contributes to j_0, while only the circular injection current

contributes to j_χ. For the Weyl nodes described by Eq. (8), injection current can be written as

$$\sigma^{abc} = -\frac{\tau_{\rm cp} e^3}{4\pi^2\hbar^2\ell^2}\int {\rm d}k_z \sum_{n,m} f_{nm}\Delta^a_{mn} r^c_{nm} r^b_{mn}\delta(\omega_{mn}-\omega), \quad (11)$$

where $\tau_{\rm cp}$ is the relaxation time of chirality-preserving scattering, $f_{nm} = f_n - f_m$ with $f_n = f(\varepsilon_n)$ being the occupation number of the nth band, $\Delta^a_{mn} = v^a_m - v^a_n$ with v^a_n being the group velocity of n band, r^c_{nm} is the interband Berry connection. Given that the linear (circular) injection current is the real (imaginary) part of the conductivity, we have $\sigma^{abc}_0 = {\rm Re}\{\sigma^{abc}\}$ and $\sigma^{abc}_\chi = {\rm Im}\{\sigma^{abc}\}$. Then $\tilde{\sigma}_0$ and $\tilde{\sigma}_\chi$ can be accessed by inserting Eq. (11) back to their definitions in Eq. (10). When node I, II, I′ or II′ is selectively activated, it is easy to show that their $\tilde{\sigma}_0$ and $\tilde{\sigma}_\chi$ possess the same magnitudes, albeit with differing signs, given the same $\hbar\omega$, B and μ. Specificlly, $\tilde{\sigma}_0({\rm I}) = \tilde{\sigma}_0({\rm II}') = \tilde{\sigma}_\chi({\rm II}) = \tilde{\sigma}_\chi({\rm II}') = -\tilde{\sigma}_0({\rm I}') = -\tilde{\sigma}_0({\rm II}) = -\tilde{\sigma}_\chi({\rm I}) = -\tilde{\sigma}_\chi({\rm I}')$.

For the Weyl node described by Eq. (8), only valid optical transitions are from Landau level $n = \mp 1$ (for $\chi = \pm 1$) to zeroth Landau level. Then the critical value for nonzero optical transitions $\hbar\omega_{\rm c}$ is given by

$$\hbar\omega_{\rm c} = \sqrt{2\hbar v_\perp^2 eB + \mu^2 \frac{v_\parallel^2}{(v_\parallel - v_t)^2}} + \mu\frac{v_\parallel}{v_\parallel - v_t}, \quad (12)$$

which is at the k_z where zeroth Landau level crosses the Fermi level. We can see that $\hbar\omega_{\rm c}$ is smaller for Weyl node with Fermi level μ lowered by chirality imbalance within a Weyl pair. Specifically, when the $E_{\rm DC}$-field is (anti-)parallel to the B-field, $\delta\mu > 0$ ($\delta\mu < 0$), and the Weyl node with $\chi = -1$ ($\chi = 1$) can be activated with a smaller $\hbar\omega_{\rm c}$. Also, it should be noted that the critical value $\hbar\omega_{\rm c}$ is same for nodes I, II, I′ and II′, given the same μ and B.

For the range of energy of light showing the switching effect to be not too small, $\delta\mu$ should be comparable to μ_0. Since $\mu_0 = -6$ meV, here we take $|\delta\mu| = 4$ meV, along with a B-field in the range from 8 T to 10 T. The Landau level spacing sets roughly the minimum energy of light (about 10 meV). In Fig. 3(a), we plot the summation of $\tilde{\sigma}_0$ over nodes I and II as a function of $\hbar\omega$ and B, given $\delta\mu = -4$ meV. The two black dashed lines represent the critical values for optical excitations of the two Weyl nodes with different chemical potentials, respectively. For a given B-field, when the energy of light is too small to excite either one of the Weyl nodes, both $\tilde{\sigma}_0$ and $\tilde{\sigma}_\chi$ are zero. When the light energy increases and meets the left black dashed line, only one Weyl node is activated for optical response while the other is Pauli blocked due to the chiral imbalance. In this case, $\tilde{\sigma}_0$ and $\tilde{\sigma}_\chi$ acquire nonzero values, the signs of which are determined by the tilt and chirality of the activated node, respectively. As light energy increases further and exceeds the right black dashed line, $\tilde{\sigma}_0$ and $\tilde{\sigma}_\chi$ are zero again since both Weyl nodes are activated. Therefore, the blue area in Fig. 3(a) corresponds to an optical response from a single activated Weyl node. The nonzero optical response outside the two black dashed lines originates from the finite relaxation time that we considered. Figure 3(b) illustrates how the total second-order DC photocurrents $j_z^{(2)}$ vary with η when node I, II, I′, or II′ is selectively activated. Their distinct behaviors demonstrate the validation of identifying the signs of j_0 and j_χ by measuring $j_z^{(2)}(\eta)$ at different η, as discussed in Eq. (10).

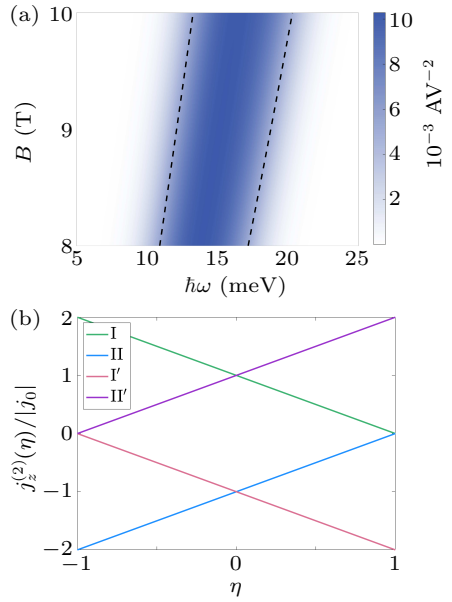


Fig. 3. Numerical demonstration of selective activation of Weyl node for photocurrent. (a) In the presence of chirality imbalance, summation of $\tilde{\sigma}_0$ over nodes I and II as $\hbar\omega$ and B vary. Dashed lines indicate the upper and lower frequency boundaries outside of which the photocurrents of two nodes cancel out. (b) When node I, II, I′ or II′ is selectively activated, total photocurrent $j_z^{(2)}(\eta)$ varies with η. The results are normalized by $|j_0|$.

Based on the discussion above, we propose ferromagnetic $MnBi_2Te_4$ as a magnetoelectrically regulated terahertz optical device, as illustrated in Fig. 4. Figure 4(a), 4(b), 4(c), or 4(d) corresponds to the configuration that node I, II, II′, or I′ is selectively activated. The direction of the B-field ($E_{\rm DC}$-field) of each configuration is indicated by purple (orange) arrows. Whether nodes I and II or nodes I′ and II′ are present is determined by the direction of the B-field. Under a given magnetic field, inverting the $E_{\rm DC}$-field leads to the change of activation of the Weyl node. Let us take Fig. 4(a) as an example to illustrate our proposal. When $E_{\rm DC}$-field is antiparallel to the B-field, $\delta\mu < 0$. Since node I has a smaller $\hbar\omega_{\rm c}$ compared to node II, it can be selectively activated as discussed in Fig. 3(a) with proper choice of parameters. In this case, the total photocurrent in z direction only comes from node I. And the direction of j_0 (j_χ) depends on the sign of tilt (chirality) of Weyl node I exclusively. By measuring $j_z^{(2)}$ at different η, we can identify the signs of j_0 and j_χ. The other configurations in Fig. 4 can be interpreted in a similar way. Therefore, by re-

versing the directions of external electromagnetic fields and selectively activating the Weyl node, we can manipulate the directions of j_0 and j_χ.

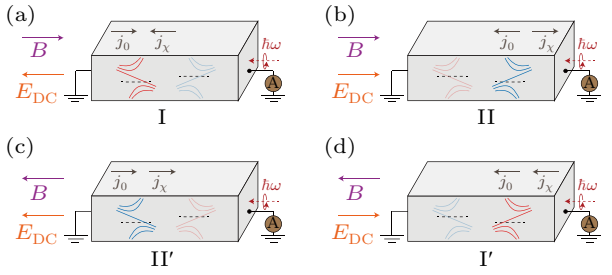


Fig. 4. Magnetoelectrically regulated photocurrents in ferromagnetic $MnBi_2Te_4$. Panels (a)–(d) respectively show the directions of the external electromagnetic fields and the directions of the photocurrents j_0 and j_χ when node I, II, II′, or I′ is selectively activated. Weyl nodes marked in dark and light colors correspond to activated and deactivated Weyl nodes, respectively. In the presence of chiral imbalance, the chemical potentials (indicated by the black dashed lines) are different within the pair of Weyl nodes.

4. Conclusion

Our study presents a systematic approach to characterize the nonlinear optical conductivity of Weyl nodes based on their tilt and chirality. We have explored how the transformations of the tilt and chirality of the Weyl node impact its nonlinear optical conductivity. We have shown that the general nth-order optical conductivity of Weyl nodes can be decomposed into a chirality-independent part σ_0 and a chirality-dependent part σ_χ. Furthermore, we have discussed how σ_0 and σ_χ respond to the change of tilt and chirality. Our approach can be used to characterize the optical conductivities of Weyl nodes and to analyze the interrelation of optical conductivities between a pair of symmetry-related Weyl nodes. Remarkably, our theory does not require a comprehensive understanding of the complete symmetry or microscopic expressions of the optical conductivities. To showcase the utility of our approach, we propose ferromagnetic $MnBi_2Te_4$ as a magnetoelectrically regulated optical device that can generate two independent photocurrent components, j_0 and j_χ. Their signs can be cooperatively controlled by the directions of the B-field and E_{DC}-field.

Appendix A: Brief introduction to length-gauge theory

In this section, we will briefly review the length-gauge theory of nonlinear optical response. And we will make examples to show why the general nonlinear optical conductivity can be expressed in the form of Eq. (3).

The perturbation of an electric field of light can be handled either in velocity-gauge or length-gauge, which are two equivalent treatments up to a unitary transformation. In the velocity-gauge, the Hamiltonian is obtained with $\boldsymbol{p}\to\boldsymbol{p}+e\boldsymbol{A}$. However, when it comes to practical calculations, velocity-gauge treatment suffers from several troublesome drawbacks.[35] On the contrast, the length-gauge theory developed by Sipe and others[22,23] is free from these drawbacks and is widely implemented in the study of nonlinear optical response. In the length-gauge, the system is perturbed by the electric dipole

$$H = H_0 + H_{\rm scat} + e\boldsymbol{r}\cdot\boldsymbol{E}(t), \tag{A1}$$

where H_0 is the unperturbed Hamiltonian, $H_{\rm scat}$ represents all the scattering effects. The electric field can be written as $\boldsymbol{E}(t) = \boldsymbol{E}^\gamma \mathrm{e}^{-\mathrm{i}\omega_\gamma t}$ in the long wavelength limit. Index γ indicates the summation over different frequency components of light and complex conjugate of certain frequency component. For example, the electric field of monochromatic light is described by $\boldsymbol{E}(t) = \boldsymbol{E}(\omega)\mathrm{e}^{-\mathrm{i}\omega t} + \boldsymbol{E}(-\omega)\mathrm{e}^{\mathrm{i}\omega t}$, where $\boldsymbol{E}^*(\omega) = \boldsymbol{E}(-\omega)$.

The vital problem of length-gauge theory lies in how to treat the position operator in the Bloch basis. The matrix elements of $\boldsymbol{r}$ are easier to handle by distinguishing its intraband part and interband part by $\boldsymbol{r} = \boldsymbol{r}_{\rm i} + \boldsymbol{r}_{\rm e}$. The matrix elements are

$$\begin{aligned}\langle n\boldsymbol{k}|r^b_{\rm i}|m\boldsymbol{k}'\rangle &= \delta_{nm}\left[\delta\left(\boldsymbol{k}-\boldsymbol{k}'\right)\xi^b_{nn} + \mathrm{i}\partial_{k_b}\delta\left(\boldsymbol{k}-\boldsymbol{k}'\right)\right],\\ \langle n\boldsymbol{k}|r^b_{\rm e}|m\boldsymbol{k}'\rangle &= \delta\left(\boldsymbol{k}-\boldsymbol{k}'\right)r^b_{nm}.\end{aligned} \tag{A2}$$

Here $|n\boldsymbol{k}\rangle$ is the Bloch state, $r^b_{nm} = (1-\delta_{nm})\xi^b_{nm}$, ξ^b_{nm} is Berry connection $\xi^b_{nm} = \langle u_{n\boldsymbol{k}}|\mathrm{i}\partial_{k_b}|u_{m\boldsymbol{k}}\rangle$, $|u_{m\boldsymbol{k}}\rangle$ is the periodic part of Bloch state. We can see that matrix elements of the intraband part are highly singular because a k_b-derivative of the Dirac delta function is involved. Fortunately, intraband part $\boldsymbol{r}_{\rm i}$ only appears in the commutators in the derivation, the matrix element of which is no longer singular,

$$\begin{aligned}\langle n\boldsymbol{k}|\left[r^b_{\rm i}, S^c\right]|m\boldsymbol{k}'\rangle &= \delta\left(\boldsymbol{k}-\boldsymbol{k}'\right)\mathrm{i}(S^c_{nm})_{;k_b}\\ (S^c_{nm})_{;k_b} &= \partial_{k_b}S^c_{nm} - \mathrm{i}(\xi^b_{nn}-\xi^b_{mm})S^c_{nm}.\end{aligned} \tag{A3}$$

Here, we require that S^c is an operator which can be easily handled like the interband of the position operator $\boldsymbol{r}_{\rm e}$.

Based on the quantum Liouville equation

$$\mathrm{i}\hbar\frac{\mathrm{d}\rho}{\mathrm{d}t} = [H,\rho] \tag{A4}$$

and discussions above, we can derive the dynamical equation in Bloch basis

$$\begin{aligned}\frac{\mathrm{d}\rho_{mn}}{\mathrm{d}t} + \mathrm{i}\omega_{mn}\rho_{mn} &= -\frac{e}{\hbar}E_b(t)(\rho_{mn})_{;k_b}\\ &+\frac{\mathrm{i}e}{\hbar}E_b(t)\sum_l\left(r^b_{ml}\rho_{ln}-\rho_{ml}r^b_{ln}\right) + \left.\frac{\mathrm{d}\rho_{mn}}{\mathrm{d}t}\right|_{\rm scat},\end{aligned} \tag{A5}$$

in which $\omega_{mn} = (\varepsilon_m - \varepsilon_n)/\hbar$ and ε_n is the energy of band n. The first term in the r.h.s. of the equation comes from the commutator of the intraband part of position operator and density

operator $[r^b_{\rm i},\rho]$, the second term comes from the commutator of the interband part of position operator and density operator $[r^b_{\rm e},\rho]$ and the third term corresponds to the density change due to scattering effects $[H_{\rm scat},\rho]$. To proceed with the discussion, the scattering effects are considered with relaxation time approximation $\mathrm{d}\rho_{mn}/\mathrm{d}t|_{\rm scat}=-\tau_{\rm s}^{-1}(\rho_{mn}-\rho^{(0)}_{mn})$, where $\tau_{\rm s}$ is the phenomenological relaxation time and $\rho^{(0)}_{mn}=\delta_{mn}f_n(\varepsilon_n)$ is the Fermi distribution. By iteratively solving this equation, we can access the density correction of each order as $\rho_{mn}=\rho^{(0)}_{mn}+\rho^{(1)}_{mn}+\rho^{(2)}_{mn}+\cdots$. For example, when we insert $\rho^{(0)}_{mn}$ into the second term of the r.h.s. of dynamical equation, we will get a density correction which is linear in electric field and can be marked as $\rho^{\rm e}_{mn}$ since it comes from the interband density correction. $\rho^{\rm e}_{mn}$ is expressed as

$$\rho^{\rm e}_{mn}=-\frac{e}{\hbar}\frac{f_{nm}r^b_{mn}}{\omega_{mn}-\omega_\gamma-\mathrm{i}\tau_{\rm s}^{-1}}E^\gamma_b\,\mathrm{e}^{-\mathrm{i}\omega_\gamma t}, \tag{A6}$$

where $f_{nm}=f_n-f_m$ is the difference of Fermi distribution between band n and m. If we insert $\rho^{\rm e}_{mn}$ into the first term of the dynamical equation, we will get a second-order density correction $\rho^{\rm ei}_{mn}$. In conclusion, we have $\rho^{(1)}_{mn}=\rho^{\rm i}_{mn}+\rho^{\rm e}_{mn}$ for linear density correction and $\rho^{(2)}_{mn}=\rho^{\rm ii}_{mn}+\rho^{\rm ie}_{mn}+\rho^{\rm ei}_{mn}+\rho^{\rm ee}_{mn}$ for second-order density correction. Higher order density corrections can be accessed in a similar way.

The expectation value of electric current is

$$j_a=-e\sum_{n,m,\boldsymbol{k}}v^a_{nm}\rho_{mn}, \tag{A7}$$

in which v^a_{nm} is the matrix elements of velocity operator.

Then, the total nth-order photocurrent with a frequency ω_n can be expressed as

$$\begin{aligned}&j^{(n)}_a(t;\omega_n)=j^{(n)}_a(\omega_n)\,\mathrm{e}^{-\mathrm{i}\omega_n t}+j^{(n)}_a(-\omega_n)\,\mathrm{e}^{\mathrm{i}\omega_n t},\\&j^{(n)}_a(\omega_n)=\sum_{C(\omega_n)}\sigma^{ab_1\cdots b_n}(\omega_n;\omega_{\gamma_1}\cdots\omega_{\gamma_n})E^{\gamma_1}_{b_1}\cdots E^{\gamma_n}_{b_n},\end{aligned} \tag{A8}$$

where $\omega_n=\omega_{\gamma_1}+\cdots+\omega_{\gamma_n}$, and $\sigma^{ab_1\cdots b_n}(\cdots)$ is the nth-order conductivity tensor. The set $C(\omega_n)$ collects all possible selections of n frequencies that sum to ω_n. The formula in the second line is the Eq. (2) in the Section 2.

Below, we take some typical optical responses induced by monochromatic light as the example to show why the general nth-order optical conductivity derived from the length-gauge theory can be written in the form of Eq. (3). Linear optical conductivity is

$$\begin{aligned}&j^{\rm opt}_a=\sigma^{ab}_{\rm opt}(\omega;\omega)E(\omega)\,\mathrm{e}^{-\mathrm{i}\omega t},\\&\sigma^{ab}_{\rm opt}=\frac{\mathrm{i}e^2}{\hbar}\int[\mathrm{d}\boldsymbol{k}]\sum_{n\neq m}f_{nm}\omega_{nm}r^a_{nm}r^b_{mn}\delta(\omega_{mn}-\omega),\end{aligned} \tag{A9}$$

in which $[\mathrm{d}\boldsymbol{k}]=\mathrm{d}^dk/(2\pi)^d$. This photocurrent comes from the resonant part of $\rho^{\rm e}_{nm}$, which corresponds to the second term of the decomposition $(\omega_{mn}-\omega-\tau_{\rm s}^{-1})^{-1}=\mathcal{P}(\omega_{mn}-\omega)^{-1}+\mathrm{i}\pi\delta(\omega_{mn}-\omega)$. $\mathcal{P}(\cdots)$ represents the principal part and $\delta(\cdots)$ indicates the Dirac delta function. Hereafter, when we introduce optical responses, the frequency dependence of the optical conductivity in the second line is omitted for brevity.

It is widely acknowledged that shift current and injection current are two contributions that dominate the second-order DC photocurrent when energy of light is larger than the band gap $\hbar\omega>E_{\rm gap}$ in the clean limit.[23,36] The shift current is

$$\begin{aligned}&j^{\rm shift}_a=\sigma^{abc}_{\rm shift}(0;\omega,-\omega)E_b(\omega)E_c(-\omega),\\&\sigma^{abc}_{\rm shift}=-\frac{\pi e^3}{2\hbar^2}\int[\mathrm{d}\boldsymbol{k}]\sum_{n,m}f_{nm}\bar{R}^a_{mn}r^c_{nm}r^b_{mn}\delta(\omega_{mn}-\omega),\end{aligned} \tag{A10}$$

in which $\bar{R}^a_{mn}=R^{a;b}_{mn}-R^{a;c}_{nm}$ and $R^{a;b}_{mn}=\mathrm{i}\partial_{k_a}\left(\log r^b_{mn}\right)+\xi^a_{mm}-\xi^a_{nn}$ is the shift vector. Shift current can be viewed as the second-order DC photocurrent that comes from the shift of the real space center of electron, when the electron in the valence band absorbs a photon and jumps into conduction band. The injection current is

$$\begin{aligned}&j^{\rm inj}_a=\sigma^{abc}_{\rm inj}(0;\omega,-\omega)E_b(\omega)E_c(-\omega),\\&\sigma^{abc}_{\rm inj}=-\frac{\tau_{\rm s}\pi e^3}{\hbar^2}\int[\mathrm{d}\boldsymbol{k}]\sum_{n,m}f_{nm}\Delta^a_{mn}r^c_{nm}r^b_{mn}\delta(\omega_{mn}-\omega),\end{aligned} \tag{A11}$$

in which $\tau_{\rm s}$ is the relaxation time, $\Delta^a_{nm}=v^a_m-v^a_n$ is the difference of group velocity between band m and n. The name injection current comes from the fact that this DC photocurrent grows linearly with illumination time within relaxation time.

Recently, it is recognized that jerk current has an important contribution to the third order DC photocurrent, when there exists a static electric field in addition to the monochromatic light.[37] The jerk current can be expressed as

$$\begin{aligned}&j^{\rm jerk}_a=\sigma^{abcd}_{\rm jerk}(0;\omega,-\omega,0)E_b(\omega)E_c(-\omega)E_d(0),\\&\sigma^{abcd}_{\rm jerk}=\frac{2\pi\tau_{\rm s}^2e^4}{\hbar^3}\int[\mathrm{d}\boldsymbol{k}]\sum_{n,m}f_{nm}\frac{\partial^2\omega_{nm}}{\partial k^a\partial k^d}r^c_{nm}r^b_{mn}\delta(\omega_{mn}-\omega),\end{aligned} \tag{A12}$$

which grows quadratically with illumination time within relaxation time.

Based on the discussions above, it is easy to see that the total nth-order photocurrent with a frequency ω_n can be expressed as Eq. (2) and a general nth-order optical conductivity can be written in the form of Eq. (3).

Appendix B: Symmetry analysis of nonlinear optical conductivity

Symmetry analysis of nonlinear optical conductivity is straightforward if the symmetry operation is purely spatial. In this case, we can directly perform tensor transformation on the nonlinear optical conductivity tensor and see the consequence of the symmetry operation. However, things become troublesome when the symmetry operation involves time-reversal

because of dissipation.[8] A proper analysis for such symmetry requires knowledge of a microscopic expression of optical conductivities. For the sake of completeness and clarity, we paraphrase how to analyze the impact of time-reversal of the nonlinear optical conductivity presented in previous literature in this section and illustrate with an example.

A general nth-order optical response can be expressed as

$$j_a^{(n)}(\tilde{\omega}_n) = \sigma^{ab_1\cdots b_n}(\tilde{\omega}_n)E_{b_1}(\tilde{\omega}_{\gamma_1})\ldots E_{b_n}(\tilde{\omega}_{\gamma_n}). \tag{B1}$$

Here we define $\tilde{\omega} = \omega + \mathrm{i}\tau_{\mathrm{s}}^{-1}$. For brevity, $\sigma^{ab_1\cdots b_n}(\tilde{\omega}_n)$ represents $\sigma^{ab_1\cdots b_n}(\tilde{\omega}_n;\tilde{\omega}_{\gamma_1}\cdots\tilde{\omega}_{\gamma_n})$. In the discussions below, when we write $\sigma^{ab_1\cdots b_n}(-\tilde{\omega}_n)$, it means $\sigma^{ab_1\cdots b_n}(-\tilde{\omega}_n;-\tilde{\omega}_{\gamma_1}\cdots-\tilde{\omega}_{\gamma_n})$.

The time-reversal counterpart of Eq. (B1) is

$$j_a'^{,(n)}(\tilde{\omega}_n) = \sigma'^{,ab_1\cdots b_n}(\tilde{\omega}_n)E'_{b_1}(\tilde{\omega}_{\gamma_1})\ldots E'_{b_n}(\tilde{\omega}_{\gamma_n}). \tag{B2}$$

To correctly describe how Eq. (B1) transforms under time-reversal Θ, the key is to realize that electric current is generally dissipative. It means that we need to additionally reverse the sign of the phenomenological relaxation time τ_{s} in order to make the decay in time to the growth in time,[8] i.e.,

$$\begin{aligned} &j_a(\tilde{\omega}_n)\to j'_a(\tilde{\omega}_n) = -j_a(-\tilde{\omega}_n),\\ &E_a(\tilde{\omega}_{\gamma_i})\to E'_a(\tilde{\omega}_{\gamma_i}) = E_a(-\tilde{\omega}_{\gamma_i}). \end{aligned} \tag{B3}$$

Equation (B2) can be further written as

$$-j_a^{(n)}(-\tilde{\omega}_n) = \sigma'^{,ab_1\cdots b_n}(\tilde{\omega}_n)E_{b_1}(-\tilde{\omega}_{\gamma_1})\cdots E_{b_n}(-\tilde{\omega}_{\gamma_n}). \tag{B4}$$

On the other hand, we can rewrite Eq. (B1) as

$$j_a^{(n)}(-\tilde{\omega}_n) = \sigma^{ab_1\cdots b_n}(-\tilde{\omega}_n)E_{b_1}(-\tilde{\omega}_{\gamma_1})\ldots E_{b_n}(-\tilde{\omega}_{\gamma_n}). \tag{B5}$$

Thus, it can be concluded that the time-reversal operation requires the optical conductivity to transform as follows:

$$\sigma'^{,ab_1\cdots b_n}(\tilde{\omega}_n) = -\sigma^{ab_1\cdots b_n}(-\tilde{\omega}_n). \tag{B6}$$

Let us take linear injection current (the part of injection current that corresponds to the g^{cb}_{nm} in the decomposition of $r^c_{nm}r^b_{mn}$) as the example to illustrate how to analyze optical conductivity under time-reversal operation. Linear injection current is

$$\sigma^{abc}_{\mathrm{inj,L}} = \frac{\tau_{\mathrm{s}}e^3}{\hbar^2}\int[\mathrm{d}\boldsymbol{k}]\sum_{n,m} f_{nm}\Delta^a_{mn}g^{cb}_{nm}\frac{\tau_{\mathrm{s}}^{-1}}{(\omega_{mn}-\omega)^2+\tau_{\mathrm{s}}^{-2}}. \tag{B7}$$

Here, we express the Dirac delta function as

$$\delta(\omega_{mn}-\omega) = \frac{1}{\pi}\frac{\tau_{\mathrm{s}}^{-1}}{(\omega_{mn}-\omega)^2+\tau_{\mathrm{s}}^{-2}}, \tag{B8}$$

for the convenience of analyzing $\tau_{\mathrm{s}}\to-\tau_{\mathrm{s}}$.

According to Eq. (B6), for the system illuminated by monochromatic light, the second-order DC optical conductivity under the time-reversal operation is

$$\sigma'^{,abc}(\tilde{\omega};\tilde{\omega}_1,\tilde{\omega}_2) = -\sigma^{abc}(-\tilde{\omega};-\tilde{\omega}_1,-\tilde{\omega}_2), \tag{B9}$$

in which $\tilde{\omega} = \tilde{\omega}_1+\tilde{\omega}_2$, $\tilde{\omega}_1 = \omega+\mathrm{i}\tau_{\mathrm{s}}^{-1}$, $\tilde{\omega}_2 = -\omega+\mathrm{i}\tau_{\mathrm{s}}^{-1}$. Then we have

$$\begin{aligned} &\sigma^{\prime,abc}_{\mathrm{inj,L}}\\ &= -\frac{(-\tau_{\mathrm{s}})e^3}{\hbar^2}\int[\mathrm{d}\boldsymbol{k}]\sum_{n,m} f_{nm}\Delta^a_{mn}g^{cb}_{nm}\frac{(-\tau_{\mathrm{s}})^{-1}}{(\omega_{mn}+\omega)^2+(-\tau_{\mathrm{s}})^{-2}}\\ &= -\frac{\tau_{\mathrm{s}}e^3}{\hbar^2}\int[\mathrm{d}\boldsymbol{k}]\sum_{n,m} f_{nm}\Delta^a_{mn}g^{cb}_{nm}\frac{\tau_{\mathrm{s}}^{-1}}{(\omega_{mn}-\omega)^2+\tau_{\mathrm{s}}^{-2}}\\ &= -\sigma^{abc}_{\mathrm{inj,L}}. \end{aligned} \tag{B10}$$

In the derivation above, the second equality takes into account the exchange of the m and n indices, as well as the symmetric property of g^{cb}_{nm} under the exchange of these indices. Through this analysis, we have verified that the linear injection current changes sign under time-reversal operation. Then we further find that linear injection current is symmetric under space–time inversion $P\Theta$, which indicates it corresponds to σ_0. Other optical conductivities can be analyzed in a similar way. Here we emphasize that, though linear injection current is identified as σ_0, linear injection current is identified as σ_χ. The correspondence between $g^{cb}_{nm}/\Omega^{cb}_{nm}$ and σ_0/σ_χ needs examination of the microscopic expression of the conductivities.

Appendix C: Extend the discussions of Eqs. (5) and (6) and Table 1 to the multi-Weyl nodes

In addition to the normal Weyl nodes described by Eq. (1) with chiral charges $\chi = \pm1$, there also exist multi-Weyl nodes that have larger chiral charges with $\chi = \pm2,\pm3$, which are protected by rotation C_4 or C_6.[25] A multi-Weyl node is generally described by[26]

$$\mathcal{H}_n = tk_z + wk_\parallel^2 + v_zk_z\sigma_z + v(k_+^n\sigma_+ + k_-^n\sigma_-). \tag{C1}$$

The eigenstates of the multi-Weyl node are $\varepsilon_s = tk_z + wk_\parallel^2 + s\sqrt{v_z^2k_z^2+v^2k_\parallel^{2n}}$, where $s=\pm1$ corresponds to conduction and valence bands, respectively. $k_\parallel = \sqrt{k_x^2+k_y^2}$ and $k_\pm = k_x \pm \mathrm{i}k_y$. The subscript $n = 2,3$ denotes the double and triple Weyl nodes, respectively. The first two terms refer to the linear and quadratic tilting terms. Contrast to the linear tilting term, the quadratic tilting term with $w>0$ ($w<0$) always pushes up (down) spectrum for any k-plane with a given k_z. When $|t|>|v_z|/|w|>|v|$, the spectrum is overtilted, leading to a type-II/type-III Weyl node.

If we want to discuss how the tilt and chirality of the multi-Weyl node affect its optical conductivity, we need to

identify the definitions of the reversal of tilt and chirality for the multi-Weyl node. According to the previous discussions, for a normal Weyl node described by Eq. (1), the chirality is reversed while the spectrum is unchanged under the space–time inversion $P\Theta$ and tilt is reversed while chirality remains unaffected under the time-reversal Θ. Since Eqs. (5) and (6) and Table 1 are equivalent to the symmetry analysis, the discussions can be generalized to the multi-Weyl node by examining how they transformed under $P\Theta$ and Θ. By doing so, chirality reversal for the multi-Weyl node can be identified as $(v_z, v) \mapsto (-v_z, (-1)^n v)$, and tilt reversal as $(t, w) \mapsto (-t, w)$.

Appendix D: Treatment of chiral anomaly at steady states

In ferromagnetic $MnBi_2Te_4$, there are only a pair of Weyl nodes. Considering a magnetic field $\boldsymbol{B} = B\hat{z}$ and a static electric field $\boldsymbol{E}_{\rm DC} = E_{\rm DC}\hat{z}$, both Weyl nodes can be described by

$$H = \mathcal{H} + H_{\text{cv-scat}} + H_{\text{cp-scat}} + e\boldsymbol{r}\cdot\boldsymbol{E}_{\rm DC}. \tag{D1}$$

Here $\mathcal{H} = H_0(\boldsymbol{k} + e\boldsymbol{a})$ with $H_0(\boldsymbol{k})$ is the effective Hamiltonian of a unperturbed Weyl node. $\boldsymbol{a}$ is the vector potential that describes the magnetic field. $H_{\text{cv-scat}}$ describes the chirality-violating scattering. $H_{\text{cp-scat}}$ describes the chirality-perserving scattering.

For a cold and clean system, the interband transition due to the static electric field $\boldsymbol{E}_{\rm DC}$ can be neglected. Then, the dynamical equations of Weyl nodes described by Eq. (A5) reduce to

$$\frac{\mathrm{d}\rho_n^\chi}{\mathrm{d}t} = -\frac{e}{\hbar}E_{\rm DC}\partial_{k_z}\rho_n^\chi + \left.\frac{\mathrm{d}\rho_n^\chi}{\mathrm{d}t}\right|_{\rm scat}, \tag{D2}$$

with $\chi = \pm$ marks the chirality of the Weyl nodes and $\rho_n^\chi \equiv \rho_{nn}^\chi$.

Considering the relaxation time approximation, we have

$$\left.\frac{\mathrm{d}\rho_n^\chi}{\mathrm{d}t}\right|_{\rm scat} = -\frac{\rho_n^\chi - \rho_n^{\chi,\rm eq}}{\tau_{\rm cp}} - \frac{1}{2}\frac{\rho_n^\chi - \rho_n^{-\chi}}{\tau_{\rm cv}}. \tag{D3}$$

The first term at the r.h.s. describes that the Weyl node tends to relax to its equilibrium distribution $\rho^{\chi,\rm eq}$. The tendency for the chiral anomaly to generate an imbalanced population between two Weyl nodes is counterbalanced by the chirality-violating scattering, which is introduced in the second term at the r.h.s. The factor $1/2$ indicates that the dynamics of a given Weyl node will contribute to half density difference between two Weyl nodes. For the steady states, we have $\mathrm{d}\rho_n^\chi/\mathrm{d}t = 0$. Then, the dynamical equation can be further written as

$$\frac{e}{\hbar}E_{\rm DC}\partial_{k_z}\rho_n^\chi = -\frac{\rho_n^\chi - \rho_n^{\chi,\rm eq}}{\tau_{\rm cp}} - \frac{1}{2}\frac{\rho_n^\chi - \rho_n^{-\chi}}{\tau_{\rm cv}}. \tag{D4}$$

Considering $\chi = +1$ and integrating over k_z on both sides of the equation, we have

$$\frac{e}{\hbar}E_{\rm DC}\frac{1}{2\pi\ell^2}\int\frac{\mathrm{d}k_z}{2\pi}\partial_{k_z}\rho_n^{+1} = -\frac{1}{2}\frac{N_n^{+1} - N_n^{-1}}{\tau_{\rm cv}}, \tag{D5}$$

where $\ell = \sqrt{\hbar/(eB)}$ is the magnetic length, the factor $1/(2\pi\ell^2)$ describes the degeneracy of the Landau level, N_n^χ is the density of the Weyl node with chirality χ and landau level n. The chirality-preserving scattering will not change the density N_n^χ, thus vanishes after integration.

For the zeroth landau level, $\partial_{k_z}\rho_0^\chi = -\chi\delta(k_z - k_{\rm F})$. Then, we have

$$N_0^{+1} - N_0^{-1} = \frac{e^2}{2\pi^2\hbar^2}\tau_{\rm cv}\boldsymbol{E}_{\rm DC}\cdot\boldsymbol{B}. \tag{D6}$$

Therefore, the density difference between two Weyl nodes is proportional to $\boldsymbol{E}_{\rm DC}\cdot\boldsymbol{B}$ and $\tau_{\rm cv}$. This density difference of zeroth level between two Weyl nodes refers to chirality imbalance due to chiral anomaly. Based on the relation between density difference and chemical potential difference,[38] the resulting chemical potential imbalance between the zeroth Landau level of the two Weyl nodes is

$$\delta\mu = \mu^+ - \mu^- = \frac{3e^2\hbar}{4\pi^2}\frac{v_\parallel v_\perp^2\tau_{\rm cv}}{\mu^2 + (\pi k_{\rm B}T)^2}\boldsymbol{E}_{\rm DC}\cdot\boldsymbol{B}. \tag{D7}$$

Since the two Weyl nodes are well-separated in momentum space, the relaxation time of the chirality-violating scattering is considered to be much larger than the relaxation time of the chirality-perserving scattering $\tau_{\rm cv} \gg \tau_{\rm cp}$. At steady states, the dynamical equations of Weyl nodes are decoupled and the effects of chiral anomaly can be considered as the shift of chemical potential $\delta\mu$. Then, the scattering term in dynamical equations are

$$\left.\frac{\mathrm{d}\rho_n^\chi}{\mathrm{d}t}\right|_{\rm scat} = -\frac{\rho_n^\chi - \rho_n^{\chi,\rm eq}}{\tau_{\rm cp}}, \tag{D8}$$

$\rho_n^{\chi,\rm eq}$ is the Fermi distribution and corresponding chemical potential is $\mu^\chi = \mu_0 + \chi\frac{\delta\mu}{2}$. μ_0 is the chemical potential of the unperturbed Wey node and $\chi\frac{\delta\mu}{2}$ is the shift of chemical potential due to chiral anomaly. Therefore, the investigation of optical response of Weyl nodes can be handled in the standard length-gauge theory if the optical electric field $E(t)$ has no contributions to the chiral anomaly.

Appendix E: Details of calculating $\tilde{\sigma}_0$ and $\tilde{\sigma}_\chi$ of Weyl nodes with Landau levels

Introducing the B-field in z-direction with vector potential $\boldsymbol{a} = Bx\hat{y}/\hbar$, the Weyl nodes in ferromagnetic $MnBi_2Te_4$ can be described by Eq. (8). Then the energy of the nth (n is an integer) Landau level at $\boldsymbol{k} = [k_y, k_z]$ is

$$\varepsilon_{n\boldsymbol{k}} = tv_t k_z + \chi\,\mathrm{sgn}(n)\eta_n, \tag{E1}$$

in which $\eta_n = \sqrt{2|n|\hbar^2 v_\perp^2/\ell^2 + \eta_\parallel^2}$ $(n \neq 0)$, $\ell = \sqrt{\hbar/eB}$ is the magnetic length, $\eta_0 = \eta_\parallel = v_\parallel k_z$, and the sign function $\mathrm{sgn}(n)$ equals -1 if $n = 0$. The corresponding wavefunction is

$$\Psi_{n\boldsymbol{k}}(x) = \frac{\mathrm{e}^{\mathrm{i}(k_y y + k_z z)}}{\sqrt{L_y L_z}} \begin{bmatrix} \mathrm{sgn}(n) u_n \psi_{|n|-1}(x') \\ \mathrm{i} w_n \psi_{|n|}(x') \end{bmatrix}, \tag{E2}$$

where $x' = x/\ell + k_y \ell$, $\sqrt{\ell}\psi_n(x)$ is the Hermite–Gaussian function, and the coefficients $u/w_n = \sqrt{\frac{1}{2}\left(1 \pm \mathrm{sgn}(n)\frac{\eta_\parallel}{\eta_n}\right)}$. The velocity matrix elements that essential for nonlinear optical conductivities are

$$\begin{aligned} v_{x,mn\boldsymbol{k}} &= \mathrm{i}\chi\tilde{v}_\perp \left[\delta_{|m|,|n|+1}\,\mathrm{sgn}(m) u_m w_n - (m \leftrightarrow n)\right], \\ v_{y,mn\boldsymbol{k}} &= \chi\tilde{v}_\perp \left[\delta_{|m|,|n|+1}\,\mathrm{sgn}(m) u_m w_n + (m \leftrightarrow n)\right], \\ v_{z,mn\boldsymbol{k}} &= \delta_{|m|,|n|}\big((\tilde{v}_t + \chi\tilde{v}_\parallel)\,\mathrm{sgn}(m)\,\mathrm{sgn}(n) u_m u_n \\ &\quad + (\tilde{v}_t - \chi\tilde{v}_\parallel) w_n w_m\big), \end{aligned} \tag{E3}$$

where $\tilde{v} = v/\hbar$. From Eq. (E3), we can see that the optical transitions are nonzero only between Landau levels that satisfy $|m| - |n| = \pm 1$.

Appendix F: Influence of topological surface states

Our work focuses on the resonant photocurrent in the terahertz frequency range under the clean limit. Typically, the energy of terahertz light is much lower than the energy gap between different surface states on a single surface, allowing us to neglect the contribution of an individual surface to the resonant photocurrent. Moreover, the photoexcitation between surface states of the top and bottom surfaces, or between surface states and bulk Weyl nodes, can also be disregarded due to the large real space separation. Under these circumstances, it is safe to consider that the response from the Weyl nodes is dominant.

In certain scenarios, the contribution from the surface may still be significant. In such cases, we can differentiate between the contributions to the nonlinear photocurrent from topological surface states and bulk states based on their differing symmetries. For instance, Ref. [39] indicates that for the RhSi system, when considering light incident perpendicular to the surface, the photocurrent from the Fermi arc is always perpendicular to the photocurrent from the bulk states.

We also emphasize that the suggested magnetoelectrically-regulated photocurrent in the ferromagnetic $MnBi_2Te_4$ is unaffected by topological surface states. In Weyl semimetals, the topological surface states known as Fermi arcs connect the projection points of two bulk Weyl nodes. In the ferromagnetic $MnBi_2Te_4$, the two Weyl nodes are located on the high-symmetry line $\bar{Z}$–Γ–Z, and their z-direction projections coincide. Therefore, the surface normal to the z-direction is topologically trivial.

In general, the differentiation of the nonlinear optical response of Fermi arcs and Weyl nodes is worth exploring. However, it goes beyond the scope of the present work and remains for future works.

Acknowledgments

Project supported by the National Key R&D Program of China (Grant Nos. 2018YFA, 0305601, and 2021YFA1400100), the National Natural Science Foundation of China (Grant Nos. 12274003, 11725415, and 11934001), and the Innovation Program for Quantum Science and Technology (Grant No. 2021ZD0302600).

References

[1] Liu J, Xia F, Xiao D, García de Abajo F J and Sun D 2020 *Nat. Mater.* **19** 830
[2] Zhang T, Ooi K J A, Chen W, Ang L K and Sin Ang Y 2019 *Opt. Express* **27** 38270
[3] Lv Y Y, Xu J, Han S, Zhang C, Han Y, Zhou J, Yao S H, Liu X P, Lu M H, Weng H, Xie Z, Chen Y B, Hu J, Chen Y F and Zhu S 2021 *Nat. Commun.* **12** 6437
[4] Takasan K, Morimoto T, Orenstein J and Moore J E 2021 *Phys. Rev. B* **104** L161202
[5] Tilmann B, Pandeya A K, Grinblat G, Menezes L D S, Li Y, Shekhar C, Felser C, Parkin S S P, Bedoya-Pinto A and Maier S A 2022 *Adv. Mater.* **34** 2106733
[6] de Juan F, Grushin A G, Morimoto T and Moore J E 2017 *Nat. Commun.* **8** 15995
[7] Chan C K, Lindner N H, Refael G and Lee P A 2017 *Phys. Rev. B* **95** 041104
[8] Ahn J, Guo G Y and Nagaosa N 2020 *Phys. Rev. X* **10** 041041
[9] Yang X, Burch K and Ran Y 2018 arXiv:1712.09363 [cond-mat]
[10] Ma J, Gu Q, Liu Y, Lai J, Yu P, Zhuo X, Liu Z, Chen J H, Feng J and Sun D 2019 *Nat. Mater.* **18** 476
[11] Wang H and Qian X 2020 *npj Comput. Mater.* **6** 199
[12] Gao Y, Zhang F and Zhang W 2020 *J. Phys.: Condens. Mat.* **32** 275502
[13] Cheng J L, Sipe J E and Wu S W 2020 *ACS Photonics* **7** 2515
[14] Morimoto T and Nagaosa N 2016 *Sci. Adv.* **2** e1501524
[15] Nagaosa N and Morimoto T 2017 *Adv. Mater.* **29** 1603345
[16] Nielsen H B and Ninomiya M 1981 *Nucl. Phys. B* **185** 20
[17] Chang G, Singh B, Xu S Y, Bian G, Huang S M, Hsu C H, Belopolski I, Alidoust N, Sanchez D S, Zheng H, Lu H, Zhang X, Bian Y, Chang T R, Jeng H T, Bansil A, Hsu H, Jia S, Neupert T, Lin H and Hasan M Z 2018 *Phys. Rev. B* **97** 041104
[18] Wan X, Turner A M, Vishwanath A and Savrasov S Y 2011 *Phys. Rev. B* **83** 205101
[19] Soluyanov A A, Gresch D, Wang Z, Wu Q, Troyer M, Dai X and Bernevig B A 2015 *Nature* **527** 495
[20] Nielsen H and Ninomiya M 1983 *Phys. Lett. B* **130** 389
[21] Fukushima K, Kharzeev D E and Warringa H J 2008 *Phys. Rev. D* **78** 074033
[22] Aversa C and Sipe J E 1995 *Phys. Rev. B* **52** 14636
[23] Sipe J E and Shkrebtii A I 2000 *Phys. Rev. B* **61** 5337
[24] Provost J P and Vallee G 1980 *Commun. Math. Phys.* **76** 289
[25] Fang C, Gilbert M J, Dai X and Bernevig B A 2012 *Phys. Rev. Lett.* **108** 266802
[26] Li X P, Deng K, Fu B, Li Y, Ma D S, Han J, Zhou J, Zhou S and Yao Y 2021 *Phys. Rev. B* **103** L081402
[27] Zhang D, Shi M, Zhu T, Xing D, Zhang H and Wang J 2019 *Phys. Rev. Lett.* **122** 206401
[28] Otrokov M M, Rusinov I P, Blanco-Rey M, Hoffmann M, Vyazovskaya A Y, Eremeev S V, Ernst A, Echenique P M, Arnau A and Chulkov E V 2019 *Phys. Rev. Lett.* **122** 107202

[29] Li J, Li Y, Du S, Wang Z, Gu B L, Zhang S C, He K, Duan W and Xu Y 2019 *Sci. Adv.* **5** eaaw5685
[30] Gu M, Li J, Sun H, Zhao Y, Liu C, Liu J, Lu H and Liu Q 2021 *Nat. Commun.* **12** 3524
[31] Lee S H, Graf D, Min L, Zhu Y, Yi H, Ciocys S, Wang Y, Choi E S, Basnet R, Fereidouni A, Wegner A, Zhao Y F, Verlinde K, He J, Redwing R, Gopalan V, Churchill H O H, Lanzara A, Samarth N, Chang C Z, Hu J and Mao Z Q 2021 *Phys. Rev. X* **11** 031032
[32] Kresse G and Furthmüller J 1996 *Phys. Rev. B* **54** 11169
[33] Perdew J P, Burke K and Ernzerhof M 1996 *Phys. Rev. Lett.* **77** 3865
[34] Lee S H, Zhu Y, Wang Y, *et al.* 2019 *Phys. Rev. Res.* **1** 012011
[35] Ventura G B, Passos D J, Lopes dos Santos J M B, Viana Parente Lopes J M and Peres N M R 2017 *Phys. Rev. B* **96** 035431
[36] Watanabe H and Yanase Y 2021 *Phys. Rev. X* **11** 011001
[37] Fregoso B M, Muniz R A and Sipe J E 2018 *Phys. Rev. Lett.* **121** 176604
[38] Li Q, Kharzeev D E, Zhang C, Huang Y, Pletikosić I, Fedorov A V, Zhong R D, Schneeloch J A, Gu G D and Valla T 2016 *Nat. Phys.* **12** 550
[39] Chang G, Yin J X, Neupert T, Sanchez D S, Belopolski I, Zhang S S, Cochran T A, Cheng Z, Hsu M C, Huang S M, Lian B, Xu S Y, Lin H and Hasan M Z 2020 *Phys. Rev. Lett.* **124** 166404